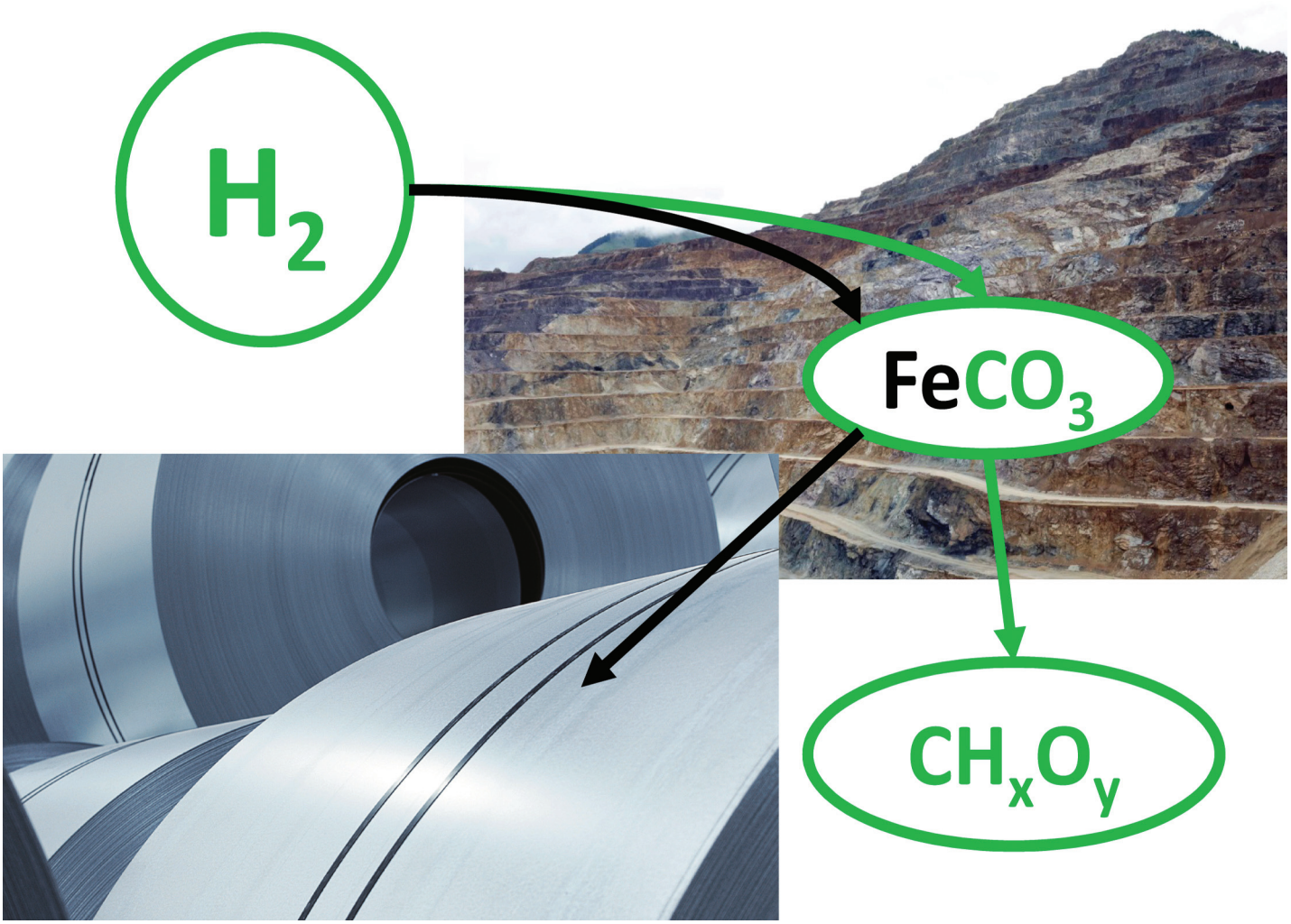

Research conducted at the Institute of Chemical Engineering and Environmental Technology in cooperation with the industrial partners VA Erzberg and voestalpine (all from Austria).

Sustainable iron production from mineral iron carbonate and hydrogen

The reduction of $FeCO_3$ with hydrogen suppresses intermediate Fe_2O_3 formation. CO_2 emission can be reduced by 60% and the amount of reducing agent can be reduced by 33% compared to state-of-the-art iron carbonate beneficiation. The kinetics and reaction mechanism of the reduction of mineral $FeCO_3$ with gaseous hydrogen were determined with a thermogravimetric method.

As featured in:

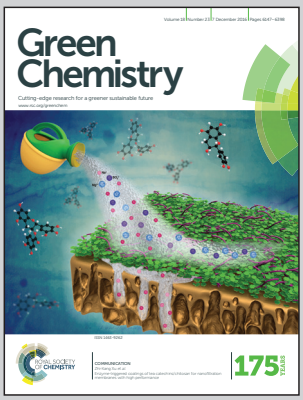

See G. Baldauf-Sommerbauer, S. Lux *et al.*, *Green Chem.*, 2016, **18**, 6255.

ROYAL SOCIETY OF CHEMISTRY

www.rsc.org/greenchem

Registered charity number: 207890

Green Chemistry

PAPER

View Article Online
View Journal | View Issue

Cite this: *Green Chem.*, 2016, **18**, 6255

Sustainable iron production from mineral iron carbonate and hydrogen

G. Baldauf-Sommerbauer,* S. Lux* and M. Siebenhofer

The reduction of iron ores with hydrogen is considered a promising CO_2 breakthrough technology to mitigate CO_2 emissions from the iron and steel industry. The state-of-the-art production of iron and steel from mineral iron carbonates ($FeCO_3$) is based on the thermal decomposition of $FeCO_3$ in air to produce hematite (Fe_2O_3) suitable for iron production. Our approach is to directly reduce $FeCO_3$ with hydrogen to elemental iron, avoiding Fe_2O_3 formation. As a consequence, CO_2 emissions can be decreased by 60% and up to 33% less reducing agent is needed for iron production. The development of environmentally benign production pathways needs to be based on a fundamental understanding of the reaction kinetics and mechanism. Therefore, thermogravimetry was used to determine the kinetics of the formation of iron from mineral iron carbonate and the concomitant decomposition of the accessory matrix carbonates of calcium, magnesium, and manganese. The isoconversional kinetic analysis according to the Ozawa–Flynn–Wall, Kissinger–Akahira–Sunose, and Friedman approach confirms the proposed parallel kinetic model. Multi-variate non-linear regression was used to determine the appropriate kinetic parameters. The conversion of iron carbonate to iron can be described with the two-dimensional Avrami-Erofeev model A2. Therefore, a temperature-controlled nucleation and diffusional growth mechanism is suggested for iron formation from mineral iron carbonate and hydrogen. The multi-parameter reaction models C*n*-X and Bna can be used to describe the concomitant iron, calcium oxide, magnesium oxide, and manganese oxide formation without applying multi-step kinetics. The multi-parameter reaction models predict a conversion above 95% at 450 °C within less than 60 minutes reaction time. Unavoidably, 1 mole of carbon dioxide is always emitted when 1 mole of $FeCO_3$ is converted into iron. Catalytic carbon dioxide hydrogenation (CCDH) can be applied to diminish inevitable CO_2 emissions by chemical conversion into value-added carbon containing chemicals. Therefore, we propose a process that combines the improved iron production *via* direct $FeCO_3$ reduction with CCDH as a follow-up reaction.

Received 3rd August 2016,
Accepted 11th October 2016

DOI: 10.1039/c6gc02160c

www.rsc.org/greenchem

Introduction

According to the Fifth Assessment Report of the Intergovernmental Panel on Climate Change (IPCC),[1] the industrial sector is responsible for approximately one third of the total anthropogenic CO_2-equivalent (CO_2^e) emissions. Iron- and steelmaking accounts for 13–25%[2,3] of these industrial CO_2^e emissions. Several approaches can contribute to a substantial decrease of CO_2^e emissions from the iron- and steel industry: (1) reduction of steel production and demand,[2] (2) increased steel recycling and scrap use,[4] and (3) innovative iron- and steelmaking technologies, also called CO_2 breakthrough technologies. Global steel production and demand is not expected to decrease within the 21st century and an increase of the share of recycled steel (= secondary steel) on total steel production can be expected.[4,5] However, to meet global industrial demand for iron based products, primary steel production from iron ores will continue to contribute a major part of the CO_2^e emissions from the global iron and steel sector. Therefore, various research programs aiming at the development of CO_2 breakthrough technologies have been initiated: ULCOS I and II in the EU, COURSE 50 in Japan, the POSCO CO_2 breakthrough framework in South Korea, and the AISI program in the USA, to mention the most extensive ones.[3,6,7] Fu *et al.*[6] and Quader *et al.*[3,8] provide an overview and evaluation of these programs. The COURSE 50, POSCO framework, and the AISI CO_2 breakthrough program explicitly include hydrogen reduction of iron ores as a key future technology. To reach a substantial decrease of anthropogenic CO_2^e emission within the 21st century most nations adopted the 'Paris Pact' that includes a commitment to the transition of the global energy sector from fossil fuels to renewables.[9] Fischedick *et al.*[5] did show that direct hydrogen reduction of iron ores is an

Graz University of Technology, NAWI Graz, Institute of Chemical Engineering and Environmental Technology, Inffeldgasse 25C, 8010 Graz, Austria.
E-mail: baldauf-sommerbauer@tugraz.at, susanne.lux@tugraz.at

environmentally and economically promising iron and steel production route in a 100% renewable energy system.

The world steel production increased from 1.53 Gt in 2013[10] to 1.60 Gt in 2015.[11]† China makes up for approximately 50% of the world steel and 57% of the world iron production.[11,12] China[13] and Austria[14] have major mineral iron carbonate (= siderite) reserves, which are used as ores for iron and steel production. Siderite beneficiation is challenging, because of the low iron content of the ore compared to magnetite and hematite ores. The industrial practice is to blend siderite with other high-grade ores in the sinter plant.[15,16] During the sintering process, siderite is converted to hematite Fe_2O_3 through roasting in air according to eqn (1). The sinter product is fed to the blast furnace where it is reduced with coal *via* CO, producing at least 1.5 mole CO_2 per mole of iron due to the stoichiometry of reaction (2). Consequently, at least 2.5 mole CO_2 are emitted during the production of 1 mole of iron from iron carbonate. The direct reduction of iron carbonate with hydrogen according to eqn (3) reduces the carbon dioxide emissions by 60% to one mole of CO_2 per mole of iron. As will be outlined in this work, the remaining CO_2 emissions can be limited by catalytic hydrogenation of carbon dioxide (CCDH)[17–19] according to eqn (4) and (5) to value added products such as methane and higher hydrocarbons *via* Fischer-Tropsch synthesis.

$$FeCO_3 + 0.25O_2 \xrightarrow{Air} 0.5Fe_2O_3 + CO_2 \quad (1)$$

$$0.5Fe_2O_3 + 1.5CO \rightarrow Fe + 1.5CO_2 \quad (2)$$

$$FeCO_3 + H_2 \rightarrow Fe + H_2O + CO_2 \quad (3)$$

$$CO_2 + 4H_2 \rightarrow CH_4 + 2H_2O \quad (4)$$

$$CO_2 + 3H_2 \rightarrow -CH_2- + 2H_2O \quad (5)$$

Improvement of siderite beneficiation has focused on innovative roasting technologies[14] and direct reduction with coal.[13,20] Neither of these processes greatly affects the CO_2 emissions and could be considered a CO_2 breakthrough technology. Nowadays (2016), most of the industrially used hydrogen is produced from fossil fuels by steam reforming ($CH_4 + H_2O \rightarrow 3H_2 + CO$) and the water-gas shift reaction ($H_2O + CO \rightarrow H_2 + CO_2$) with natural gas as the primary feedstock. At least 0.25 moles of CO_2 are produced per mole of hydrogen in combined steam reforming and water-gas shift (eqn (6)).

$$CH_4 + 2H_2O \rightarrow 4H_2 + CO_2 \quad (6)$$

Even when the hydrogen supply of direct carbonate reduction (eqn (3)) is covered by combined steam reforming and water-gas shift (eqn (6)), the stoichiometric CO_2 emission per mole of iron is decreased by 50% compared to roasting of iron carbonate and subsequent reduction. Renewable and sustainable hydrogen production is extensively investigated.[21–26] The production of 'green' hydrogen is not only conceivable from a scientific point of view, but also necessary from an environmental point of view to meet the global CO_2 mitigation targets for the 21st century.

The detailed understanding of the reaction mechanism and kinetics of the fundamental reactions is the basis for the design of an environmentally benign industrial process. The kinetics for the direct hydrogen reduction of hematite Fe_2O_3 and magnetite F_3O_4 have been broadly investigated and discussed in literature.[27–30] The decomposition kinetics of mineral iron carbonate have been investigated in oxygen atmosphere,[31–33] vacuum,[34] and nitrogen atmosphere.[35–38] However, the direct reduction of mineral iron carbonate lacks kinetic and mechanistic investigation.

In this paper, we propose a kinetic model and a suggested reaction mechanism for the direct hydrogen reduction of mineral iron carbonate to elemental iron on the basis of thermogravimetric experiments. Based on the reaction kinetics developed in this work, a process concept and an outlook to a carbon dioxide utilization approach by coupling direct hydrogen reduction of iron carbonate with catalytic carbon dioxide hydrogenation (CCDH) to value added products (*e.g.* methane, methanol, higher hydrocarbons) is presented.

Experimental and computational methods

Thermogravimetric measurements were performed on a Netzsch Jupiter STA 449C balance with alumina sample pans. Hydrogen and nitrogen were used in 99.999% quality (AirLiquide). The X-ray diffraction (XRD) spectra were recorded on a Panalytical X'Pert Pro diffractometer equipped with a cobalt radiation tube (Co-Kα line at 0.178901 nm). The High Score Plus software together with the Inorganic Crystal Structure Database was used for compound determination. The quantitative analysis was performed by means of Inductively Coupled Plasma-Optical Emission Spectroscopy (ICP-OES) using a Spectro Ametek Spectro Arcos device.

Sample preparation for quantitative ICP-OES analysis

2.15 g of the concentrated siderite sample was reduced on the thermobalance in 70 vol% hydrogen at a total flow rate of 100 $cm^3\ min^{-1}$. The sample was heated to 725 °C at a linear heating rate of 3 °C min^{-1} and kept at 725 °C until a constant mass was reached, indicating complete reaction. The reaction product was dissolved in a mixture of concentrated hydrochloric and concentrated nitic acid ($HCl : HNO_3 = 3 : 1$, volumetric) for elemental analysis.

Kinetic computations

Four different linear heating rates (1.8, 3, 5, 10 °C min^{-1}) were used to generate a data set suitable for kinetic computations according to the recommendations of the International Committee of Thermal Analysis and Calorimetry (ICTAC) Kinetics Committee.[39,40] Before the data collection was started, a temperature calibration was performed at a linear heating rate of

† 39 countries which account for approximately 99% (BF) and 90% (DIOR) of the world production were considered in the calculation.

5 °C min^{-1} and a nitrogen flow of 100 cm^3 min^{-1} with indium, tin, bismuth, zinc, and aluminum standard reference materials. A blank measurement was recorded every time the experimental conditions were changed and all kinetic measurements were replicated with a sample amount of 20 ± 2 mg for each run. The conversion α was calculated as the ratio of mass loss at temperature T and maximum mass loss of the experiment.

The model-free integral Ozawa–Flynn–Wall (OFW, eqn (7))[41,42] and Kissinger–Akahira–Sunose (KAS, eqn (8))[43] methods and the differential Friedman method[44] (eqn (9)) were used to check the suitability and separability of single step kinetic models.

$$\ln \beta_i = \text{const} - 1.052\frac{E_\alpha}{R_{\text{gas}} T_{\alpha,i}} \tag{7}$$

$$\ln\left[\frac{\beta_i}{T_{\alpha,i}^2}\right] = \text{const} - \frac{E_\alpha}{R_{\text{gas}} T_{\alpha,i}} \tag{8}$$

$$\ln\left[\frac{\mathrm{d}\alpha}{\mathrm{d}t}\right]_{\alpha,i} = \ln(f(\alpha)A_\alpha) - \frac{E_\alpha}{R_{\text{gas}} T_{\alpha,i}} \tag{9}$$

β_i – heating rate of the i-th temperature program, E_α – activation energy determined with a model-free method, A_α – frequency factor determined with a model-free method, α – conversion, i – temperature program, R_{gas} – ideal gas constant, T – temperature, t – time, $f(\alpha)$ – reaction model, const – an arbitrary constant.

The multi-variate regression analysis presented by Opfermann[45] implemented in the software Thermokinetics 3.1 was used for the computation of an accurate combination of Arrhenius temperature dependency $k(T)$ and reaction model $f(\alpha)$ for the general kinetic equation depicted in eqn (10).

$$\frac{\mathrm{d}\alpha}{\mathrm{d}t} = \beta \times \frac{\mathrm{d}\alpha}{\mathrm{d}T} = k(T) \times f(\alpha) = A \times e^{\frac{-E_a}{R_{\text{gas}}T}} \times f(\alpha) \tag{10}$$

α – conversion, t – time, β – linear heating rate, T – temperature, A – frequency factor, E_a – Arrhenius activation energy, $f(\alpha)$ – reaction model (see Table 1).

Evaluation of the suitability of models was done by computation of the coefficient of regression R according to eqn (11) and performing the F-test according to eqn (12).

$$R = \sqrt{1 - \frac{\sum_{i=1}^{h}\sum_{j=1}^{v}\left(y_{ij} - y_{\text{calc},ij}\right)^2}{\sum_{i=1}^{h}\left(\sum_{j=1}^{v} y_{ij}^2 - \frac{\left(\sum_{j=1}^{v} y_{ij}\right)^2}{v}\right)}} \tag{11}$$

$$F(d_A, d_B) = \frac{\sum_{i=1}^{h}\sum_{j=1}^{v} {d_A}^{-1}\left(y_{ij} - y_{\text{calc},ij}(\text{model A})\right)^2}{\sum_{i=1}^{h}\sum_{j=1}^{v} {d_B}^{-1}\left(y_{ij} - y_{\text{calc},ij}(\text{model B})\right)^2} \tag{12}$$

β – heating rate, h – number of linear heating rate scans (= 4), v – number of data points, y – measured value, y_{calc} – calculated value, d_A – degrees of freedom for model A, d_B– degrees of freedom for model B.

Results and discussion

Comparison of direct iron carbonate reduction to the state-of-the-art from a thermodynamic point of view

Iron carbonate minerals are beneficiated industrially by roasting in air to produce hematite Fe_2O_3 (eqn (1)). Reduction of hematite with hydrogen requires 1.5 moles of hydrogen per mole of iron produced (eqn (13)), whereas the direct reduction of iron carbonate requires one mole of hydrogen per mole of iron produced (eqn (3)).

$$0.5Fe_2O_3 + 1.5H_2 \rightarrow Fe + 1.5H_2O \tag{13}$$

Thus, the effectiveness of the reduction process is enhanced by 33% less reducing agent consumption when the hematite route (eqn (1) and (2)) is bypassed by direct iron car-

Table 1 Reaction models[39,45] considered in the analysis of the kinetic datasets

Code	Description	Model equation $f(\alpha)$
F1	Reaction of first order	$1-\alpha$
F2	Reaction of second order	$(1-\alpha)^2$
Fn	Reaction of n^{th} order	$(1-\alpha)^n$
R2	Two-dimensional phase boundary/contracting cylinder	$2(1-\alpha)^{1/2}$
R3	Three-dimensional phase boundary/contracting sphere	$3(1-\alpha)^{2/3}$
D1	One-dimensional diffusion	$1/(2\alpha)$
D2	Two-dimensional diffusion	$[-\ln(1-\alpha)]^{-1}$
D3J	Jander three-dimensional diffusion	$3/2 \times (1-\alpha)^{2/3}[1-(1-\alpha)^{1/3}]^{-1}$
D3GB	Ginstling-Bronstein three-dimensional diffusion	$3/2 \times [(1-\alpha)^{-1/3}-1]^{-1}$
B1	Prout-Tompkins equation	$\alpha(1-\alpha)$
Bna	Expanded Prout-Tompkins equation	$\alpha^r(1-\alpha)^n$
C1-X	First order autocatalytic reaction with catalysis by final or intermediate product X expressed as function of α	$(1-\alpha)(1+K_{\text{cat}} \times \text{X}(\alpha))$
Cn-X	n^{th} order autocatalytic reaction with catalysis by final or intermediate product X expressed as function of α	$(1-\alpha)^n(1+K_{\text{cat}} \times \text{X}(\alpha))$
A2	Avrami-Erofeev two-dimensional nucleation	$2(1-\alpha)[-\ln(1-\alpha)]^{1/2}$
A3	Avrami-Erofeev three-dimensional nucleation	$3(1-\alpha)[-\ln(1-\alpha)]^{2/3}$
An	Avrami-Erofeev n^{th} dimensional nucleation	$n(1-\alpha)[-\ln(1-\alpha)]^{(n-1)/n}$

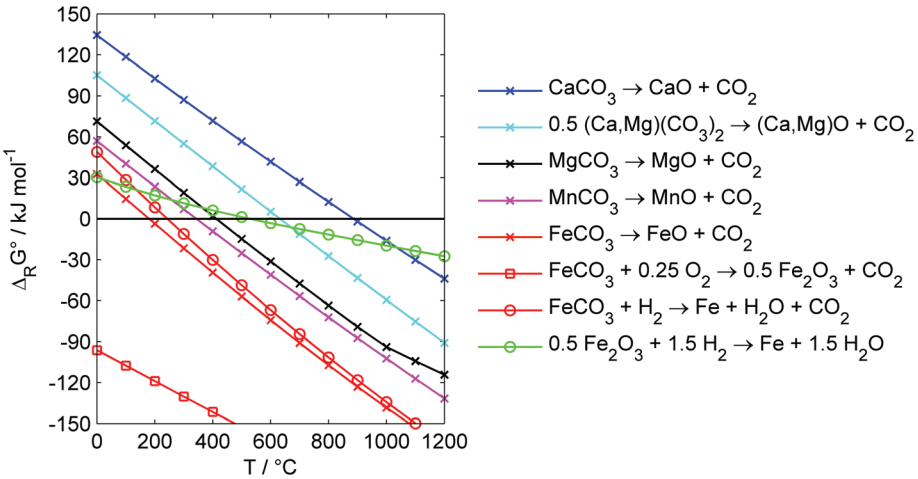

Fig. 1 Standard free energy of reaction $\Delta_R G°$ at ambient pressure calculated with HSC Chemistry 8 for the most stable solid phases. Roasting of iron carbonate (red squares) produces stable products, thus exhibits strongly negative values for $\Delta_R G°$. The reduction of iron carbonate (red circles) is thermodynamically favored over the reduction of hematite (green circles) at temperatures above 200 °C. Decomposition of carbonates to bivalent oxides is expected to proceed in the order iron (red x) < manganese (magenta x) < magnesium (black x) < dolomite (cyan x) < calcite (blue x).

bonate reduction (eqn (3)). The reduction of iron carbonate is favored over the hematite reduction at temperatures above 100 °C, due to the decreasing run of the standard free energy of reaction $\Delta_R G°$ with temperature (see Fig. 1: green line with circles for hematite, red line with circles for iron carbonate).

Mineral iron carbonates are often accompanied by calcium, magnesium, and manganese carbonates. Iron, calcium, magnesium, and manganese can either be present as separate carbonate phases or as solid solutions. The thermodynamic analysis for the carbonates shows, that $\Delta_R G°$ decreases linearly with temperature for $CaCO_3$, $(Ca,Mg)(CO_3)_2$, $MgCO_3$, $MnCO_3$, and $FeCO_3$. The temperature needed for high conversions increases in the order $FeCO_3$ < $MnCO_3$ < $MgCO_3$ < $(Ca,Mg)(CO_3)_2$ < $CaCO_3$.

Reactant and product characterization

The original mineral from the Austrian Erzberg was provided by VA Erzberg GmbH. This mineral consists of three main carbonate components: siderite $FeCO_3$ with partial Mg and Mn substitution, ankerite $(Ca_aFe_bMg_cMn_d)CO_3$, and dolomite $(Ca,Mg)(CO_3)_2$. Potassium, aluminum, and silicon are present in the form of muscovite $KAl_2(AlSi_3O_{10})(OH)_2$, whereas major parts of the silicon can be found as quartz SiO_2 (see Fig. 2a for XRD spectrum and Table 2 for composition). A 100–200 μm size fraction of the original mineral was sorted by density and separated electromagnetically in the isodynamic field. This procedure produced a concentrated siderite specimen (referred to as CS, see Fig. 2b and Table 2), which was used for the kinetic analysis.

The iron carbonate content of the CS is converted to elemental iron (79 ± 2 wt%, see Table 2) after reduction with hydrogen. Calcium, magnesium, and manganese carbonates are converted to oxides. Summation of the produced Fe, CaO, MgO, MnO, SiO_2, and Al_2O_3 results in 102 ± 3 wt% (see last row of column P in Table 2). Consequently, the conversion can be considered quantitative.

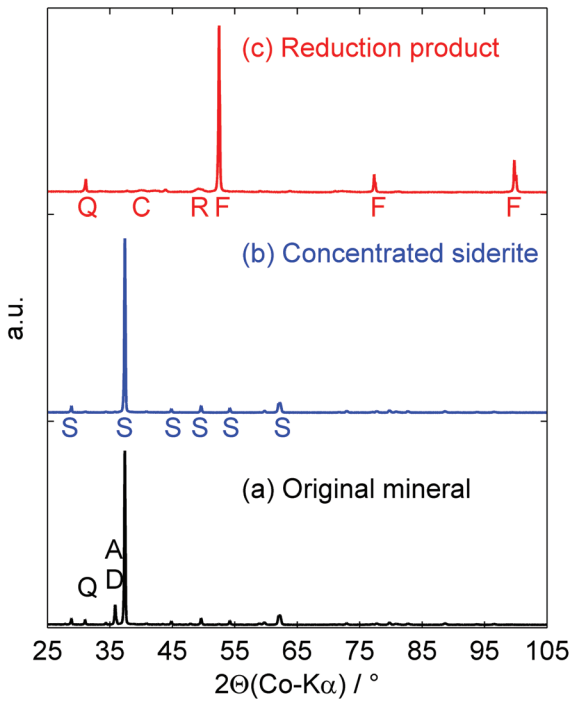

Fig. 2 XRD pattern of the original mineral from Erzberg/Austria (a), the concentrated siderite (b), and the product of the reduction of the concentrated siderite with H_2 (c). Magnesium and manganese oxide cannot be distinguished, as both oxides are present in amounts below 7wt%. The most intensive reflection for both oxides should appear at 48–50° but cannot be separated, as there is a broad peak ranging from 48.2–50.6° at this scattering angle. A: ankerite $(Ca_aFe_bMg_cMn_d)CO_3$; C: calcite, CaO; D: dolomite $(Ca,Mg)(CO_3)_2$; F: iron, Fe; R: magnesium/manganese oxide, MgO/MnO; S: siderite $FeCO_3$; Q: quartz, SiO_2.

Table 2 Results of the ICP-OES analysis (OM: original mineral, CS: concentrated siderite phase, P: product of the reduction of CS with hydrogen). Compared to the OM, the relative iron content of CS is increased and the relative content of calcium and magnesium are decreased. The reduction of CS with hydrogen yields a product with high iron content by quantitative carbonate reduction (see eqn (3))

	OM/wt% ±3% rel.	CS/wt% ±3% rel.	P/wt% ±3% rel.
Fe	33.5	39.9	79.0
CaO	5.8	1.3	2.7
MgO	3.9	3.3	6.6
MnO	2.6	3.1	5.7
SiO_2	5.4	2.1	4.7
Al_2O_3	1.1	1.5	2.9
SUM	52.3	51.2	101.6

Kinetic modelling

On the basis of the analysis of reactants and products, a parallel reaction scheme can be assumed to model the kinetics of the reduction of the concentrated mineral siderite. Iron carbonate is converted to iron (eqn (3)) and the metal carbonates of calcium, magnesium, and manganese are converted to oxides (eqn (14)).

$$FeCO_3 + H_2 \xrightarrow{k_1(T),f_1(\alpha)} Fe + H_2O + CO_2 \quad (3)$$

$$(Ca_xMg_yMn_z)CO_3 \xrightarrow{k_2(T),f_2(\alpha)} xCaO + yMgO + zMnO + CO_2 \quad (14)$$

The theoretical mass loss of the solid phase transformed in reaction (3) and (14) can be calculated from the reactant composition (see column CS in Table 2). The mass loss for the direct hydrogen reduction of the iron carbonate content of the concentrated siderite $\Delta m_{FeCO_3,Fe}$ accounts for 42.8 ± 1.3 wt% (eqn (15)). The mass loss for the conversion of the Ca-, Mg-, and Mn-carbonates to oxides $\Delta m_{MCO_3,MO}$ sum up to 6.5 ± 0.2 wt% (eqn (16)). Thus, the fractional conversion for total iron carbonate reduction $\alpha_{Fe,calc}$ can be calculated from eqn (17) and accounts for 0.87 ± 0.03. These calculated values are in good agreement with the experimental thermogravimetric curves, as depicted in Fig. 3.

$$\Delta m_{FeCO_3,Fe} = wf_{FeCO_3} \times \frac{MW(CO_3)}{MW(FeCO_3)} \quad (15)$$

$$\Delta m_{MCO_3,MO} = wf_{MCO_3} \times \frac{MW(CO_2)}{MW(MCO_3)} \quad (16)$$

$$\alpha_{Fe,calc} = \frac{\Delta m_{FeCO_3,Fe}}{\Delta m_{FeCO_3,Fe} + \Delta m_{MCO_3,MO}} \quad (17)$$

$\Delta m_{FeCO_3,Fe}$ – mass loss for the direct hydrogen reduction of the iron carbonate content of CS to iron, wf_i – mass fraction of compound i, MW(i) – molecular weight of compound i, $\alpha_{Fe,calc}$ – fractional conversion for total iron carbonate reduction.

Model-free kinetic analysis

The Ozawa–Flynn–Wall (OFW),[41,42] Kissinger–Akahira–Sunose (KAS),[43] and Friedman[44] approach result in a model-free activation energy E_α *vs.* conversion α plot (Fig. 4). If activation energy is roughly constant with the extent of reaction, the process can be described with one single step model. If two or more clearly separable E_α regimes can be observed, two or more step reactions seem to be appropriate approaches. Results from model-free E_α calculations can be used as input parameters for linear and non-linear model fitting purposes[39,46] and analysis of the variation of activation energy with extent of conversion.[46] The differential Friedman method can be applied to any temperature program, but is sensitive to experimental noise. The OFW and KAS methods do not tend to magnify experimental noise, as they are integral. But both methods introduce a systematic error in the value of model-free activation energy E_α due to the method of integration.[46] Therefore, a combinatorial interpretation of the outcome of

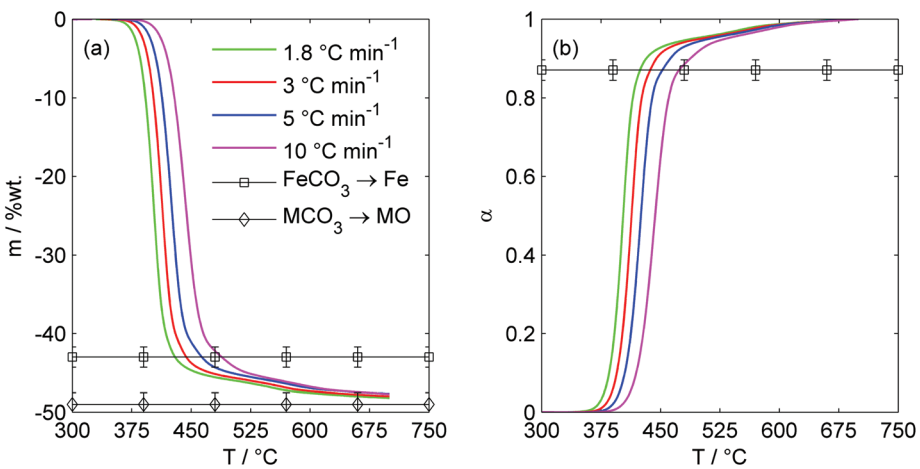

Fig. 3 Thermogravimetric curves (a) and conversion α curves (b) used for the kinetic analysis. The calculated mass loss for the reduction of iron carbonate to iron (square) and for the decomposition of the Ca-, Mg-, and Mn-carbonate (diamond) are marked. The calculated total conversion (diamond) and the experiment (a) are in good agreement. Sample mass = 20 ± 2 mg, 100 cm^3 min^{-1} total flow, 70vol% hydrogen at the inlet.

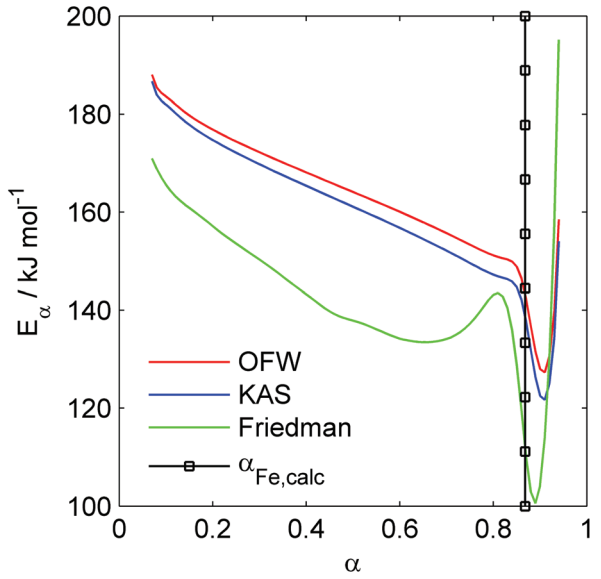

Fig. 4 Model-free activation energy E_α calculated with the Ozawa–Flynn–Wall[41,42] (OFW, red), the Kissinger–Akahira–Sunose (KAS, blue),[43] and Friedman[44] (green) approach. The shoulder starting at $\alpha \approx 0.80–0.83$ indicates the overlap of a second reaction. The black line with squares at $\alpha = 0.87$ demarks the calculated partial mass loss (0.87 ± 0.03) for complete iron carbonate conversion to iron $\alpha_{Fe,calc}$ and the start for the decomposition of Ca-, Mg-, and Mn-carbonate calculated from the sample composition.

these three methods should give a sound model-free kinetic analysis.

The OFW and KAS analysis produce a comparable result, whereas the KAS method leads to slightly lower E_α values (2–3 kJ mol^{-1}, see Table 3). This can be expected from the different temperature integral approximation (eqn (7) and (8)). The calculations based on the Friedman approach result in a comparable run of E_α *vs.* conversion. Nevertheless, the value of E_α is systematically lower (17–25 kJ mol^{-1}, see Table 3) than the value for E_α calculated with the OFW and KAS method. The three model-free approaches result in the same trend of the model-free activation energy with extent of conversion. E_α is relatively constant from $\alpha = 0.1$ to $\alpha = 0.8$ and decreases by approximately 25 kJ mol^{-1}. In theory, reactions following single step kinetics result in constant values for E_α over the whole conversion range. The constant decrease over a specific conversion range can be expected for heterogeneous mineral systems. This variation of activation energy is an indication for partially overlapping reactions, resulting in an effective, conversion dependent activation energy.[46]

The shoulder starting at $\alpha \approx 0.80$ (Friedman) and $\alpha \approx 0.85$ (OFW, KAS) indicates the overlapping start of the second reaction. As shown in Fig. 4, the occurrence of the shoulder is in good agreement with the fractional conversion for total iron carbonate reduction $\alpha_{Fe,calc} = 0.87 \pm 0.03$. Hence, the model free kinetic analysis confirms the assumed kinetic model of two parallel reactions: the reduction of iron carbonate to iron (eqn (3)) and the decomposition of Ca-, Mg-, and Mn-carbonate (eqn (14)).

Determination of a reaction model $f(\alpha)$ and proposed reaction mechanism

A multivariate non-linear regression analysis[45] of 16 commonly used single step reaction models (Table 1) was performed on the conversion range $\alpha = 0.01–0.99$ to find suitable reaction models. As shown in Table 4 and Fig. 5, the multi-parameter n^{th}-order autocatalysis model C*n*-X and the expanded Prout-Tompkins model Bna can adequately describe the whole conversion range. The model parameters (Table 4), however, are not very plausible for single step kinetics. A fractional reaction order of 2.65 (C*n*-X) and 2.56 (Bna) is an indication for overlapping reactions, as expected from the model-free analysis. Nevertheless, C*n*-X and Bna can adequately describe the concomitant conversion of iron carbonate to iron and the decomposition of the matrix carbonates of Ca, Mg, and Mn to oxides without applying multi-step kinetics (see Fig. 5).

The multi-parameter models C*n*-X and Bna are helpful for global kinetics calculations broadly used in chemical reaction engineering applications, *e.g.* reactor design. Insight into intrinsic kinetics and reaction mechanism, though, is easier achieved by applying simpler models with physico-chemical background. As shown in the plot of the standard free reaction energy (Fig. 1), reduction of iron carbonate according to eqn (3) is expected to proceed at lower temperatures than the decomposition of magnesium, manganese, and calcium car-

Table 3 Model-free activation energy E_α calculated with the Friedman (FM), Ozawa–Flynn–Wall (OFW), and Kissinger–Akahira–Sunose (KAS) method

	E_α/kJ mol^{-1}		
α	FM	OFW	KAS
0.1	164 ± 3	184 ± 1	182 ± 1
0.4	143 ± 7	168 ± 2	165 ± 3
0.5	138 ± 8	164 ± 3	161 ± 3
0.7	134 ± 9	156 ± 4	152 ± 4
0.8	143 ± 4	151 ± 5	147 ± 5
0.9	104 ± 10	128 ± 5	122 ± 5

Table 4 Results of the regression analysis for single step kinetics in the conversion range $\alpha = 0.01–0.99$. 16 commonly used reaction models for solid state kinetics were considered; see Table 1 for model description and equations. The correlation coefficient (R, see eqn (16)) and the F-test (F, see eqn (17)) are used for model comparison. Critical F-value = 1.11

Model	R	F	E_a, kJ mol^{-1}	$\log_{10}(A)$, s^{-1}	Model parameters
C*n*-X	0.9977	1.00	164.3	8.374	$n = 2.652$, $\log_{10}(K_{cat}) = 2.340$, autocatalysis by product: X = α
Bna	0.9972	1.26	163.7	10.58	$n = 2.566$, $r = 0.819$
A*n*	0.9874	5.56	162.3	9.546	$n = 1.554$
A2	0.9859	6.22	151.8	8.751	
F*n*	0.9829	7.53	201.9	12.55	$n = 1.08$

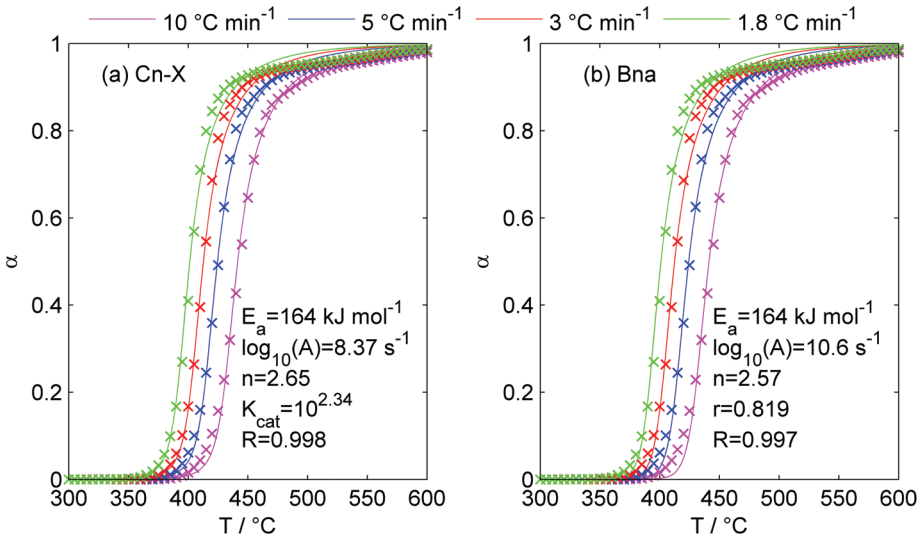

Fig. 5 Model prediction (solid lines) and experimental (x) conversion of CS into iron and conversion of calcium, magnesium, and manganese carbonate to the corresponding oxides at four different heating rates. The multi-parameter models considering autocatalysis (a: C*n*-X) and the expanded Prout-Tompkins model (b: Bna) accurately predict the experimental curves.

Table 5 Dependency of the correlation coefficient R, the activation energy E_a, and frequency factor A on the evaluated conversion range for the two-dimensional Avrami-Erofeev model A2 and the n^{th}-order model F*n*

	A2: $f(\alpha) = 2(1-\alpha)[-\ln(1-\alpha)]^{1/2}$			Fn: $f(\alpha) = (1-\alpha)^n$			
α	R	E_a, kJ mol^{-1}	$\log_{10}(A)$, s^{-1}	R	E_a, kJ mol^{-1}	$\log_{10}(A)$, s^{-1}	n
0.01–0.80	0.9976	170.1	10.27	0.9768	185.4	11.23	0.000116
0.01–0.83	0.9983	168.1	10.11	0.9797	183.1	11.03	0.000213
0.01–0.85	0.9986	166.6	9.98	0.9824	182.4	10.97	0.00445
0.01–0.87	0.9987	164.9	9.84	0.9848	180.8	10.83	0.000153
0.01–0.90	0.9980	162.2	9.61	0.9868	177.5	10.56	0.000153
0.01–0.99	0.9859	151.8	8.75	0.9830	201.8	12.55	1.084

bonate (see eqn (14)). This behavior, expected from thermodynamics, can be experimentally confirmed by the shape of the thermogravimetric curves shown in Fig. 3. The iron carbonate reduction is represented by a distinct mass loss Δm_{TG1} below 450 °C, which is followed by small relative mass loss Δm_{TG2} spanning over a broad temperature range (450–650 °C). The second mass loss Δm_{TG2} can be allocated to the concomitant decomposition of manganese, magnesium, and calcium carbonate. This proposed reaction mechanism is confirmed by the results of the model-free kinetics analysis. The shoulder in the E_α *vs.* α plot of the model-free analysis at a conversion of 0.8–0.9 (Fig. 4) is a strong indication for two separable, independent reactions. Thus, a limitation of the evaluated conversion range for model regression should result in an improvement of the goodness of fit for simple reaction models that describe the single step iron carbonate reduction according to eqn (3).

Table 3 shows that the n^{th}-dimensional Avrami-Erofeev models A*n* and the n^{th} order model F*n* produced the best results for single step kinetic models. For both models, the evaluation range for the regression analysis was gradually reduced to α = 0.8 (Table 5). The dimension n_{AE} of the A*n* model converged to 2, as the evaluated conversion range was reduced. For the F*n* model, on the contrary, the order n diverged from approximately one for α = 0.01–0.99 to values below 0.01 for α = 0.01–0.80/0.90. Therefore, the A2 model was further investigated and compared to the F*n* model in Table 5. E_a and A show a clear increasing tendency with increasing conversion range for the A2 model. E_a and A for the F*n* model, however, decrease when the upper limit of the conversion range α_u is increased from 0.80 to 0.90 but increase between α_u = 0.90 and α_u = 0.99. The correlation coefficient R is significantly higher for the A2 model compared to the F*n* model in all evaluated conversion ranges shown in Table 5. As a result, the Avrami-Erofeev two dimensional nucleation model A2 is superior to the F*n* model in describing the kinetics of the reduction of iron carbonate to iron with hydrogen.

The regression coefficient for the A2 model shows an optimum when the upper boundary of the conversion range $\alpha_{u,opt}$ is between 0.85 and 0.87 (Fig. 6 and Table 5). This range of $\alpha_{u,opt}$ coincides with the fractional conversion for complete iron carbonate reduction $\alpha_{Fe,calc}$ = 0.84–0.90 calculated from

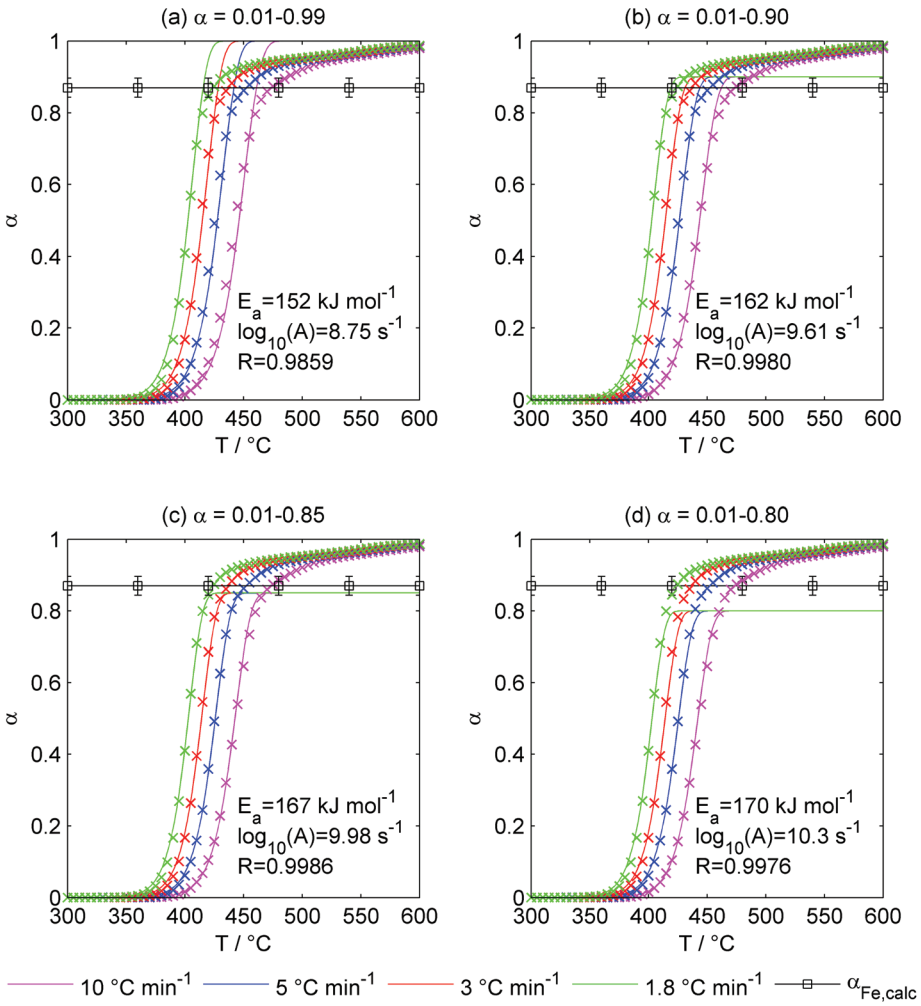

Fig. 6 Validation of the two-dimensional Avrami-Erofeev model A2 (solid lines) with the experimental TG curves (crosses). The adaption of the evaluated conversion range leads to an optimum between α = 0.85. (c) and α = 0.90 (d) of the regression coefficient R in the range of the calculated complete conversion of iron carbonate to iron $\alpha_{Fe,calc}$ (black line with squares and error bar). Experimental conditions for TG: 20 ± 2 mg, 100 cm^3 min^{-1} total inlet gas flow (70% H_2 + 30% N_2).

the elemental analysis (Fig. 6). Gotor *et al.*[34] state that n_{AE} = 2 describes two reaction mechanisms, depending on the reaction temperature. At low reaction temperatures, nuclei are formed at a constant rate and grow by one-dimensional diffusion. At elevated reaction temperatures, nucleation can be considered instantaneous and growth of nuclei proceeds by two-dimensional diffusion. Thus, it can be concluded that the formation of iron from iron carbonate *via* hydrogen reduction proceeds *via* nucleus formation and diffusional growth of nuclei. Nucleus formation and diffusional growth can be controlled by the reaction temperature.

Process concept and comparison to the state-of-the-art

The C*n*-X model parameters found in the regression analysis can be used to predict the shape and trend of the conversion of CS according to eqn (3) and (14) with time at fixed temperature (Fig. 7). After the same reaction time, conversion increases with temperature. Even at temperatures that can be considered to be low for metallurgical processes, *e.g.* 450 °C, industrially relevant conversions of more than 95% can be obtained within less than 60 minutes reaction time. For comparison, the Midrex© process for direct iron oxide reduction (DIOR) with natural gas is run at 780–900 °C (ref. 47) and a typical blast furnace (BF) is run at more than 1500 °C.[16]

Direct hydrogen reduction of mineral iron carbonates can save up to 33% of the reducing agent compared to the established iron production routes (BF, DIOR) due to the abolition of sinter production (= roasting in air, eqn (1)). Due to its magnetic properties, iron can be easily separated from MgO, MnO, CaO, and SiO_2 by magnetic separation (Fig. 8) and processed in the steel mill. The off-gas of the reduction reactor, as depicted in Fig. 8, consists of carbon dioxide, water, and excess hydrogen if the reduction reactor is run at $n(H_2) : n(FeCO_3) > 1$.

By virtue of its chemical nature conversion of iron carbonate into iron is always coupled to the emission of 1 mole of

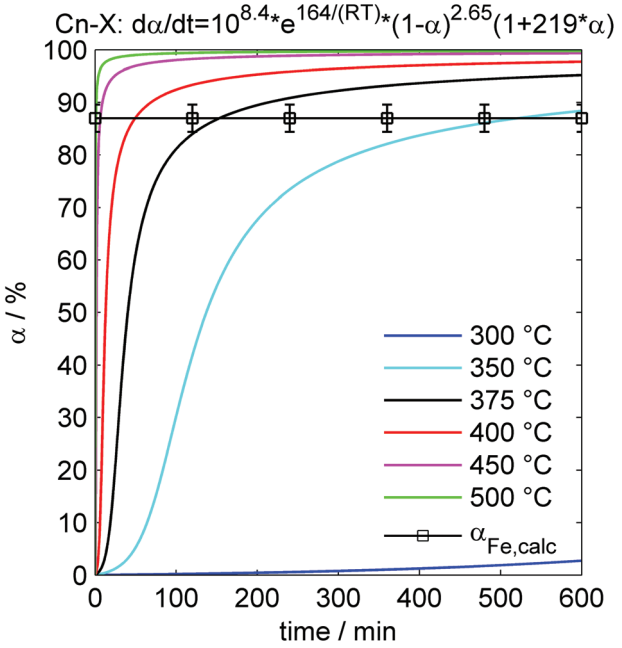

Fig. 7 Prediction of the conversion α of CS into iron and Ca-, Mg-, and Mn-oxide based on the C*n*-X model with the best parameters found in the regression analysis. At a total conversion of 87 ± 3%, quantitative iron carbonate conversion to iron ($\alpha_{Fe,calc}$) can be expected, the remaining 13 ± 3% of conversion are attributed to the conversion of calcium, magnesium, and manganese carbonate to the respective oxide.

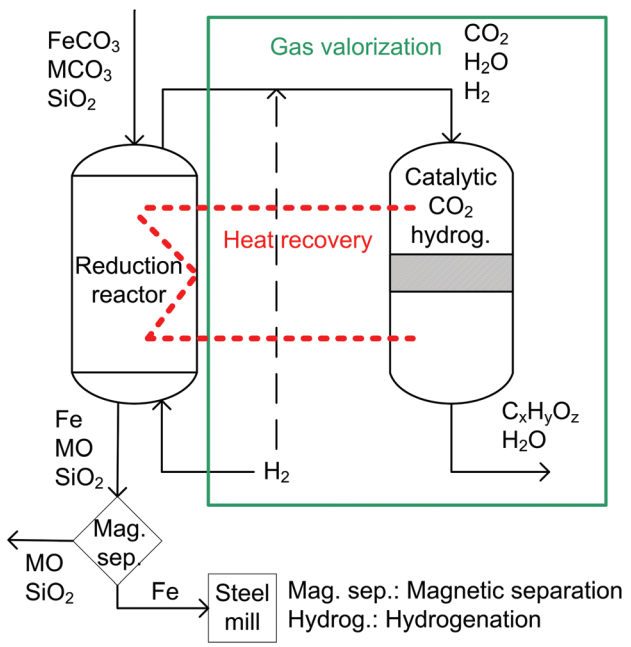

Fig. 8 Process concept for the direct hydrogen reduction of mineral iron carbonate coupled to catalytic carbon dioxide hydrogenation.

CO_2 per mole of iron produced (eqn (3)). Two possible ways for carbon dioxide mitigation are conceivable: (1) carbon capture and storage and (2) carbon dioxide utilization. Carbon dioxide utilization is preferable, as this could possibly add value to the whole process. Owing to the fact, that hydrogen is already used for iron carbonate reduction and available on-site, catalytic carbon dioxide hydrogenation (CCDH) is suggested (green frame in Fig. 8). The reduction reactor shown in Fig. 8 can either be run with the stoichiometric amount of hydrogen ($n(H_2) : n(FeCO_3) = 1$), or with excess hydrogen for the CCDH reactor. A variety of products is accessible with CCDH:[17–19] methanol, methane, higher hydrocarbons *via* Fischer-Tropsch-Synthesis, *etc*. Evaluation of the most suitable final product depends on environmental and economic factors and is out of the scope of this paper. Moreover, heat recovery can be achieved by transferring the heat of reaction produced in exothermal CCDH reactions, for instance methane synthesis (eqn (10)) or higher hydrocarbon formation *via* RWGS and Fischer-Tropsch synthesis (eqn (11)), to the reduction reactor.

$$CO_2 + 4H_2 \rightarrow CH_4 + 2H_2O \quad \Delta_R H_{573\,K} = -177\ \text{kJ mol}^{-1} \quad (4)$$

$$CO_2 + 3H_2 \rightarrow -CH_2^- + 2H_2O \quad \Delta_R H_{573\,K} = -128\ \text{kJ mol}^{-1} \quad (5)$$

Baldauf-Sommerbauer *et al.*[48] could show that reductive calcination of mineral magnesium carbonate in 90% hydrogen produces a temperature- and pressure-dependent mixture of CO, CH_4, and CO_2. Jagadeesan *et al.* revealed that synthetic $(Fe,Ca)(CO_3)_2$ can be directly converted into methane[49] and C1–C3 hydrocarbons[50] when heated to 300–600 °C in 100% H_2 flow. Thus, it can be expected that partial conversion of carbon dioxide into CO, CH_4, and/or higher hydrocarbons is possible already in the reduction reactor.

Conclusions

The production of iron and steel is one of the most energy- and emission-intensive industrial branches worldwide. Consequently, CO_2 breakthrough technologies have to be developed and improved to substantially decrease the CO_2^e emission from this sector. The direct hydrogen reduction of mineral iron carbonate was proven feasible and can be considered such a breakthrough technology that could foster green steelmaking. Multi-parameter kinetic models (C*n*-X, Bna) can be applied to predict the conversion of mineral iron carbonate into iron and matrix calcium, magnesium, and manganese carbonate into oxides. The iron carbonate reduction to iron can be described with the two-dimensional Avrami-Erofeev A2 model. As a consequence, a temperature controlled nucleation and diffusional growth mechanism for iron formation from iron carbonate in hydrogen atmosphere is proposed. Compared to the state-of-the-art, iron carbonate beneficiation *via* direct hydrogen reduction can save up to 60% of the CO_2 emissions and 33% of the reducing agent. Compared to other metallurgical iron carbonate beneficiation processes (BF, DIOR), direct hydrogen reduction can be run at relatively low (400–500 °C) temperatures. Furthermore, a concept is outlined to recycle inevitably produced carbon

dioxide by catalytic carbon dioxide hydrogenation (CCDH). Exothermal CCDH reactions can provide the necessary heat for direct hydrogen reduction of mineral iron carbonate.

Abbreviations and symbols

AISI	American iron and steel institute
BF	Blast furnace
BOF	Blast oxygen furnace
CCDH	Carbon dioxide hydrogenation
CS	Concentrated siderite
CO_2^e	Carbon dioxide equivalent
COURSE 50	CO_2 ultimate reductions in steelmaking process by innovative technology for cool earth 50
DIOR	Direct iron oxide reduction
ICP-OES	Inductively coupled plasma optical emission spectroscopy
IPCC	Intergovernmental panel on climate change
KAS	Kissinger–Akahira–Sunose
MCO_3	Calcium, magnesium, and manganese carbonate present in OM
MO	Calcium, magnesium, and manganese oxide produced from MCO_3 present in OM
OFW	Ozawa–Flynn–Wall
OM	Original mineral
P	Product
POSCO	Pohang iron and steel company
R	Correlation coefficient
TG	Thermogravimetry
ULCOS	Ultra-low carbon dioxide steelmaking
XRD	X-ray diffraction
α	Conversion
$\alpha_{Fe,calc}$	Fractional conversion for total iron carbonate reduction (eqn (9))
A_α, s^{-1}	Frequency factor determined with a model-free/isoconversional method
A, s^{-1}	Frequency factor
β_i, K min^{-1}	Heating rate of the i^{th} temperature program
$\Delta_R G°$, kJ mol^{-1}	Standard free energy of reaction
$\Delta_R H_T$, kJ mol^{-1}	Reaction enthalpy at temperature T and 1.013 bar
Δm, %	Mass change: negative for loss, positive for gain
Δm_{TGi}, %	Mass change for i^{th} step of the thermogravimetric curve
$\Delta m_{FeCO_3,Fe}$, %	Mass loss for the direct hydrogen reduction of the iron carbonate content of CS to iron
$\Delta m_{MCO_3,MO}$, %	Mass loss for the conversion of Ca-, Mg-, and Mn-carbonates of CS to oxides
d_i	Degrees of freedom for model i
E_α, kJ mol^{-1}	Model-free/isoconversional activation energy
E_a, kJ mol^{-1}	Activation energy
$f(\alpha)$	Reaction model
h	Number of linear heating rate scans
$k(T)$, K s^{-1}	Arrhenius temperature dependency: $k(T) = A^* e^{\frac{-E_a}{RT}}$
K_{cat}	Parameter for autocatalysis model Cn-X
m, wt%	Mass
MW, g mol^{-1}	Molecular weight
n	Reaction order
n_{AE}	Parameter for Avrami-Erofeev reaction model
r	Parameter for expanded Prout-Tompinks model Bna
R_{gas}, J mol^{-1} K^{-1}	Ideal gas constant
T, °C/K	Temperature
T, min	Time
v	Number of data points
y	Measured value
wf_i, %	Mass fraction of compound i

Acknowledgements

The project 'Reduzierende Kalzinierung' is funded by the Austrian 'Klima- und Energiefond' in the framework of the program 'ENERGY MISSION AUSTRIA'. The authors wish to thank Dr H. Schmid (voestalpine Stahl GmbH, Austria) and Dr A. Stadtschnitzer (VA Erzberg GmbH, Austria) for their valuable collaboration in the course of the project 'Reduzierende Kalzinierung'. The authors gratefully acknowledge the support from the NAWI Graz program. Thanks are also due to W. Aniser for his support in the performance of the experiments.

Notes and references

1 IPCC, *Climate Change 2014 Synthesis Report*, Geneva, 2014.
2 J. M. Allwood, J. M. Cullen and R. L. Milford, *Environ. Sci. Technol.*, 2010, **44**, 1888–1894.
3 M. A. Quader, S. Ahmed, R. A. R. Ghazilla, S. Ahmed and M. Dahari, *Renewable Sustainable Energy Rev.*, 2015, **50**, 594–614.
4 S. Pauliuk, R. L. Milford, D. B. Mu and J. M. Allwood, *Environ. Sci. Technol.*, 2013, **47**, 3448–3454.
5 M. Fischedick, J. Marzinkowski, P. Winzer and M. Weigel, *J. Cleaner Prod.*, 2014, **84**, 563–580.
6 J. Fu, G. Tang, R. Zhao and W. Hwang, *J. Iron Steel Res. Int.*, 2014, **21**, 275–281.
7 N. Pardo and J. A. Moya, *Energy*, 2013, **54**, 113–128.
8 M. Abdul Quader, S. Ahmed, S. Z. Dawal and Y. Nukman, *Renewable Sustainable Energy Rev.*, 2016, **55**, 537–549.
9 United Nations Framework Convention on Climate Change FCCC/CP/2015/L.9, *Adoption of the Paris Agreement*, Paris, 2015.
10 U. N. Conference on Trade and Development, *Iron ore statistics 2013*, New York/Geneva, 2013.

11 Monthly crude steel production 2015 and 01-06/2016, http://www.worldsteel.org/statistics/statistics-archive/monthly-steel-archive.html (accessed July 2016).
12 Monthly crude steel production 2015 and 01-06/2016, http://p://www.worldsteel.org/statistics/statistics-archive/monthly-steel-archive.html (accessed July 2016).
13 D. Zhu, X. Zhou, J. Pan and Y. Luo, *Miner. Process. Extr. Metall. Rev.*, 2014, **123**, 246–250.
14 A. Boehm, M. Boehm and A. Kogelbauer, *Chem. Ing. Tech.*, 2014, **86**, 883–890.
15 F. Oeters, M. Ottow, D. Senk, A. Beyzavi, J. Gunther, H. B. Lungen, M. Kolternmann and A. Buhr, *Ullmann's Encycl. Ind. Chem.*, 2011, **19**, 578–655.
16 H. B. Lüngen and J.-I. Yagi, *Ullmann's Encycl. Ind. Chem.*, 2012, **19**, 657–707.
17 I. Dimitriou, P. García-Gutiérrez, R. H. Elder, R. M. Cuéllar-Franca, A. Azapagic and R. W. K. Allen, *Energy Environ. Sci.*, 2015, **8**, 1775–1789.
18 M. D. Porosoff, B. Yan and J. G. Chen, *Energy Environ. Sci.*, 2016, 62–73.
19 W. Wang, S. Wang, X. Ma and J. Gong, *Chem. Soc. Rev.*, 2011, **40**, 3703–3727.
20 D. Zhu, Y. Luo, J. Pan and X. Zhou, *High Temp. Mater. Processes*, 2016, **35**, 185–194.
21 G. Gahleitner, *Int. J. Hydrogen Energy*, 2013, **38**, 2039–2061.
22 S. Dutta, *J. Ind. Eng. Chem.*, 2013, **20**, 1148–1156.
23 R. Chaubey, S. Sahu, O. O. James and S. Maity, *Renewable Sustainable Energy Rev.*, 2013, **23**, 443–462.
24 K. Christopher and R. Dimitrios, *Energy Environ. Sci.*, 2012, **5**, 6640.
25 O. Bičáková and P. Straka, *Int. J. Hydrogen Energy*, 2012, **37**, 11563–11578.
26 T. Abbasi and S. A. Abbasi, *Renewable Sustainable Energy Rev.*, 2011, **15**, 3034–3040.
27 A. Pineau, N. Kanari and I. Gaballah, *Thermochim. Acta*, 2006, **447**, 89–100.
28 A. Pineau, N. Kanari and I. Gaballah, *Thermochim. Acta*, 2007, **456**, 75–88.
29 H. Zuo, C. Wang, J. Dong, K. Jiao and R. Xu, *Int. J. Miner., Metall. Mater.*, 2015, **22**, 688–696.
30 F. Chen, Y. Mohassab, S. Zhang and H. Y. Sohn, *Metall. Mater. Trans. B*, 2015, **46**, 1133–1145.
31 A. P. Dhupe and A. N. Gokarn, *Int. J. Miner. Process.*, 1990, **28**, 209–220.
32 D. Alkaç and Ü. Atalay, *Int. J. Miner. Process.*, 2008, **87**, 120–128.
33 S. B. Jagtap, A. R. Pande and A. N. Gokarn, *Int. J. Miner. Process.*, 1992, **36**, 113–124.
34 F. Gotor, M. Macias, A. Ortega and J. Criado, *Phys. Chem. Miner.*, 2000, 495–503.
35 V. Y. Zakharov and Z. Adonyi, *Thermochim. Acta*, 1986, **102**, 101–107.
36 Y.-L. Pang, G.-X. Xiao and S.-W. Jiu, *Xi'an Jianzhu Keji Daxue Xuebao/J. Xi'an Univ. Archit. Technol.*, 2007, **39**, 136–139.
37 Z. L. Feng, Y. Yu, G. Liu and W. Chen, *Wuhan Ligong Daxue Xuebao/J. Wuhan Univ. Technol.*, 2009, **31**, 11–14.
38 Z. Feng, Y. Yu, G. Liu and W. Chen, *J. Wuhan Univ. Technol., Mater. Sci. Ed.*, 2011, **26**, 523–526.
39 S. Vyazovkin, A. K. Burnham, J. M. Criado, L. A. Pérez-Maqueda, C. Popescu and N. Sbirrazzuoli, *Thermochim. Acta*, 2011, **520**, 1–19.
40 S. Vyazovkin, K. Chrissafis, M. L. Di Lorenzo, N. Koga, M. Pijolat, B. Roduit, N. Sbirrazzuoli and J. J. Suñol, *Thermochim. Acta*, 2014, **590**, 1–23.
41 T. Ozawa, *Bull. Chem. Soc. Jpn.*, 1965, **38**, 1881–1886.
42 J. H. Flynn and L. A. Wall, *J. Res. Natl. Bur. Stand., Sect. A*, 1966, **70A**, 487.
43 T. Akahira and T. Sunose, *Res. Rep. Chiba Inst. Technol. (Sci. Technol.)*, 1971, **16**, 22–31.
44 H. L. Friedman, *J. Polym. Sci., Part C: Polym. Symp.*, 1964, **6**, 183–195.
45 J. Opfermann, *J. Therm. Anal. Calorim.*, 2000, **60**, 641–658.
46 S. Vyazovkin, *Phys. Chem. Chem. Phys.*, 2016, **18**, 18643–18656.
47 L. Formanek, F. Rose and J. Prölß, *Ullmann's Encycl. Ind. Chem.*, 2013, **20**, 1–14.
48 G. Baldauf-Sommerbauer, S. Lux, W. Aniser and M. Siebenhofer, Chem. Eng. Technol., 2016, in press, DOI: DOI: 10.1002/ceat.201600094.
49 D. Jagadeesan, M. Eswaramoorthy and C. N. R. Rao, *ChemSusChem*, 2009, **2**, 878–882.
50 D. Jagadeesan, Y. Sundarayya, G. Madras and C. N. R. Rao, *RSC Adv.*, 2013, **3**, 7224–7229.